Combined texture and microstructure analysis of deformed crystals by high-energy X-ray diffraction

Hao Yuan, Zhe Chen, Thomas Buslaps, Veijo Honkimaki, András Borbély

Combined texture and microstructure analysis of deformed crystals by high-energy X-ray diffraction

Hao Yuan,[a] Zhe Chen,[b] Thomas Buslaps,[c] Veijo Honkimäki[c] and András Borbély[a]*

[a]Univ. Lyon, IMT Mines Saint-Etienne, Centre SMS, CNRS, LGF, F - 42023 Saint-Etienne, France, [b]State Key Laboratory of Metal–Matrix Composites, Shanghai Jiao Tong University, Shanghai 200240, People's Republic of China, and [c]European Synchrotron Radiation Facility, Grenoble, France. *Correspondence e-mail: borbely@emse.fr

It is shown that high-energy X-ray diffraction allows a fast and accurate texture and microstructure analysis of crystals, which can help to set up optimal industrial procedures for materials manufacturing. This paper presents the experimental and theoretical aspects of quantitative texture analysis using high-energy synchrotron beams. Intensity corrections are less important in this approach than in classical laboratory methods; however, the most important correction, related to the Lorentz factor, can introduce relative fraction changes of up to about 40% compared to the uncorrected case. The resolution of the orientation density function also influences the results. For example, the usual 5° resolution leads to relative deviations of up to 30% in the fraction of some components. The method allowed detection of small changes taking place during the recovery and continuous recrystallization of a cold-rolled Al–TiB_2 nanocomposite. Texture information was combined with the results of line profile analysis, evidencing the evolution of the average dislocation density and coherent domain size of the selected grain families. It was found that recovery, as described in terms of dislocation annihilation and coherent domain coarsening, takes place at similar rates in all components.

1. Introduction

The physical properties of polycrystalline materials used in engineering components depend on their microstructure, which is usually tailored through thermomechanical processing to match the needs of the application. Particular criteria are typically formulated in terms of material conditioning (such as work hardened or recrystallized state) and/or in terms of crystallographic texture, which makes X-ray diffraction (XRD) a well suited tool for their characterization. Because of its orientation sensitivity and nondestructive character, XRD has, however, the extra potential of quantifying microstructural heterogeneity, enabling a better understanding of the polycrystal response to processing conditions. A typical example is the combined characterization of crystallographic texture (Kocks *et al.*, 2000) and the dislocation density of different texture components by line profile analysis (LPA) (Groma *et al.*, 1988; Kužel & Klimanek, 1988; Borbély & Groma, 2001; Borbély & Ungár, 2012). There are already several papers in the scientific literature dealing with this coupled problem, where the focus was mainly set on LPA (Borbély *et al.*, 2000; Guiglionda *et al.*, 2004; Csiszár *et al.*, 2012; Wauthier-Monnin *et al.*, 2015). Most of the work conducted *ex situ* delivered relevant information on microstructure evolution but less insight into the kinetics of studied phenomena, which requires *in situ* studies.

Using a laboratory X-ray source coupled to an area detector, Kühbach *et al.* (2015) have recently proposed an *in*

situ method for continuous tracking of primary recrystallization kinetics in selected single texture components of an Al–Fe–Si alloy. The method exploited the correlation between the diffracted intensity and the volume fraction of a particular texture component. The setup was optimized for high intensity, helping the recrystallization study, but the large amount of instrumental broadening (induced by the filtered $K\alpha$ radiation with a broad bandpass) prevented the evaluation of dislocation density by means of LPA. This made the approach insensitive to recovery, the phenomenon which precedes recrystallization. Ideally, a characterization method capturing both processes would be used. It is evident that the envisaged method requires high X-ray flux (for temporal resolution) and sufficient monochromaticity (for LPA), which are only available at synchrotron sources. Here, we present the potential for combined texture and LPA studies of the setup available at ID31 of the European Synchrotron Radiation Facility (ESRF) in Grenoble (Honkimäki, 2016). We show that by using a monochromatic high-energy synchrotron beam relevant texture and microstructural information from the bulk of millimetre-sized specimens can be obtained. Texture and LPA measurements were performed during *in situ* annealing of a cold-rolled Al–0.2Sc–0.1Zr alloy containing 5 wt% of TiB_2 nanoparticles (Tang *et al.*, 2015).

2. Experimental method

2.1. Description of the diffraction geometry

Fig. 1 shows a schematic drawing of the setup available at ID31. It is the simplest possible geometry containing the specimen, a goniometer with a single rotation axis and an area detector. The X-ray source is an in-vacuum cryo-cooled undulator with 14.5 mm period (U14), which provides the highest intensity in the energy range 20–150 keV. For measurements, an energy of 63 keV was selected using a double Laue–Laue monochromator with a relative bandpass of $\Delta E/E = 10^{-4}$. The diffracted intensity was measured with a PILATUS3 X CdTe 2M area detector (1475 × 1679 pixels, pixel size of 172 µm) mounted on a movable arm supported by horizontal granite beams fixed on the top of granite pillars (Honkimäki, 2016). The detector can be moved by about 8 m along the beam, ±1 m sideways, and down and up by 344 and 844 mm, respectively. The long movement along the beam allows an easy change between the low- and high-resolution modes required for texture and peak profile measurements, respectively. During scanning, the sample was rotated around the vertical axis (Oz) (ω rotation) and transmission diffraction peaks corresponding to lattice planes (hkl) fulfilling Bragg's law were recorded with the area detector. The sample-to-detector distance at the near field was determined from texture measurement considerations, namely the availability of enough diffraction rings for a high-resolution orientation density function (ODF) evaluation. We emphasize that collecting diffraction frames with several complete Debye rings leads to a higher number of diffraction vectors and high-resolution texture characterization, which also makes the pole figure inversion procedure more accurate. The presence of texture on the acquired diffraction frames is usually visible by intensity variations along the azimuthal direction of the Debye rings (described here by the angle η), as well as by the

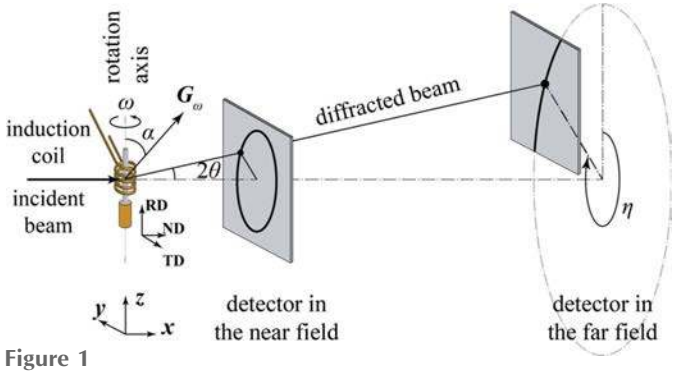

Figure 1
Schematic drawing of the experimental setup used for combined texture and microstructure analysis of deformed crystals. In low-resolution mode (used for texture mapping) the detector is placed in the near field. The high-resolution mode (used for line profile measurement) is obtained by moving the detector to the far field.

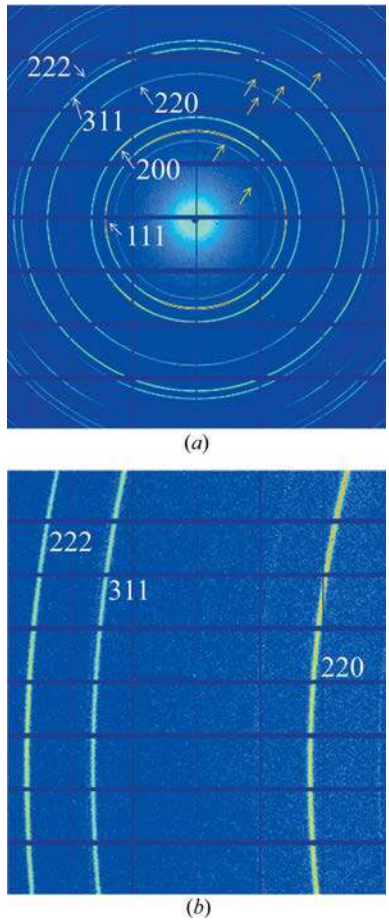

Figure 2
Diffraction frames recorded in the near field (*a*) and in the far field (*b*) on the cold-rolled Al–0.2Sc–0.1Zr–5 wt%TiB_2 nanocomposite. The first five complete Debye rings of the Al matrix are visible. The rings marked by yellow arrows belong to the TiB_2 phase. The horizontal and vertical stripes with zero intensity correspond to blind regions between detector modules.

variation at a given position $(2\theta, \eta)$ as a function of the rotation angle ω.

For measuring high-angular-resolution peaks, the detector has to be moved to the far field. Owing to the reduced field of view, it should be positioned at specific locations, which depend on the texture component and the corresponding diffraction peaks *hkl* selected for characterization. The optimal detector distance can be determined from the pixel size and the divergence of the incident beam. In the present case the beam divergence was about 14 mrad, which would allow positioning of the detector at 12 m from the sample. The selected distance based on intensity considerations was, however, shorter by 6 m. Figs. 2(*a*) and 2(*b*) show typical diffraction frames recorded at close and far distances, respectively.

2.2. Texture extraction

2.2.1. Link between texture and three-dimensional X-ray diffraction. Heidelbach *et al.* (1999) published general equations relating the detector pixel coordinates $(2\theta, \eta, \omega)$ to pole figure (PF) coordinates (ψ, φ) (where ψ is the polar angle to the normal direction, and φ is the azimuth measured from the rolling direction, in the rolling plane). Their work discusses the case with two tilt/rotation axes aligned perpendicular to the beam, which is more complex than the setup discussed here containing a single rotation axis. The latter is easier to implement in practice and can provide a better temporal resolution for *in situ* studies. With this simplification the setup becomes identical to that used in three-dimensional X-ray diffraction (3DXRD) (Poulsen, 2004), for which reason we choose the equations of the latter to transform the diffraction images into pole figures. Texture evaluation using the single-axis setup has already been described by Kocks *et al.* (2000) and by Brokmeier & Yi (2017). However, the cited work did not present all the details of the analysis. Here, we use the theoretical approach of 3DXRD, which helps a better understanding of the required intensity corrections and at the same time emphasizes that texture, as a volume-weighted orientation distribution, represents only a subset of the more general information available in 3DXRD. In the latter method, besides crystallographic orientation and volume of the grains, their centre-of-mass position and the strain tensor prevailing in each single grain can also be determined (Oddershede *et al.*, 2010; Renversade & Borbély, 2017).

In the case of using a broad synchrotron beam (1×0.5 mm, for example) the outcome of a 3DXRD measurement is usually determined by whether individual grains can be indexed or not. Non-deformed and slightly deformed coarse-grain polycrystals (with grain size greater than 100 µm) generally can be indexed, but for highly deformed specimens the azimuthal peak overlap hinders single-grain identification. In such cases only a statistical evaluation of grain orientations present in the aggregate can be obtained in terms of the ODF. To calculate the ODF, experimental PFs should be first extracted from the recorded diffraction frames, which can be done by assigning a diffraction vector $\mathbf{G}_\omega$ to each pixel or to small regions of interest (ROIs) defined on the detector (the index ω signifies the diffraction frame corresponding to the rotation angle ω of the turntable). According to Poulsen (2004), $\mathbf{G}_\omega$ is related to a reciprocal lattice point $\mathbf{H} = [h, k, l]^{\mathrm{T}}$ of the diffracting grain/subgrain volume as

$$\mathbf{G}_\omega = \mathbf{\Omega}_z \mathbf{S} \mathbf{U}^{-1} \mathbf{B} \mathbf{H}, \tag{1}$$

where $\mathbf{B}$ is the transformation matrix of $\mathbf{H}$ from the reciprocal lattice to a Cartesian system linked to the direct lattice (Busing & Levy, 1967). $\mathbf{U}$ and $\mathbf{S}$ describe the sample positioning on the ω turntable, $\mathbf{U}$ being the orientation matrix of the grain (defined here according to the passive convention) and $\mathbf{S}$ describing the relation between the sample frame (usually defined by the rolling, transverse and normal directions: RD, TD, ND) and the laboratory frame *Oxyz*. If RD, TD and ND are aligned along *Ox*, *Oy* and *Oz*, respectively (Fig. 1) $\mathbf{S} = \mathbf{I}$, *i.e.* the identity matrix. Finally, $\mathbf{\Omega}_z$ describes the rotation of the sample around *Oz*, which at ID31 was aligned perpendicular to the beam (in the vertical direction). Considering an ideal setup with the area detector perpendicular to the incident beam, the diffraction vector $\mathbf{G}_\omega$ can be expressed in terms of detector coordinates 2θ and η as (Moscicki *et al.*, 2009)

$$\mathbf{G}_\omega = \frac{1}{\lambda} \begin{bmatrix} \cos(2\theta) - 1 \\ -\sin(2\theta)\sin(\eta) \\ \sin(2\theta)\cos(\eta) \end{bmatrix}. \tag{2}$$

According to this equation the magnitude of the diffraction vector is $|\mathbf{G}_\omega| = (2\sin\theta)/\lambda$. If single-grain reflections can be separated and indexed, equations (1) and (2) can be used for 3DXRD analysis. If the grains cannot be indexed the evaluation will be restricted to the texture information, which is obtained according to the following procedure. On the basis of equation (1), the pole density in the sample coordinate system is calculated by rotating back the diffraction vector $\mathbf{G}_\omega$ corresponding to each detector ROI to the laboratory frame by $\mathbf{\Omega}_z^{-1}$, with a subsequent transformation to the sample frame by $\mathbf{S}^{-1}$:

$$\mathbf{G}_{\mathrm{S}} = \mathbf{S}^{-1} \mathbf{\Omega}_z^{-1} \mathbf{G}_\omega. \tag{3}$$

Then the integrated intensity of the ROI is associated with this vector. The details for calculating the pole figure angles (ψ, φ) corresponding to detector coordinates $(2\theta, \eta, \omega)$ are presented in the supporting material for sample setting $\mathbf{S} = \mathbf{I}$.

2.2.2. Intensity corrections. Pole figure construction needs several corrections. Therefore, the diffraction setup should be first calibrated, which was done using a NIST certified CeO_2 powder (SRM 674b) and custom-written MATLAB (The Mathworks Inc., Natick, MA, USA) routines (Renversade & Borbély, 2017) implementing the procedure described by Borbély *et al.* (2014). The fitted parameters given in Table S1 of the supplementary material indicate that the detector is almost perpendicular to the beam and equation (2), which is valid for the ideal geometry, can be applied in the present case. Setup calibration was only performed at the beginning of the beamtime; for later measurements the detector position given by the motor encoders has been accepted. The encoders have accuracies of ±1 µm in the horizontal direction and ±5 µm in

the vertical direction as well as along the beam. These are much smaller than the pixel size and introduce negligible shifts in the position of the peaks, without influencing the peak shape or texture results. After calibration the radial diffraction patterns (intensity *versus* 2θ) for each η interval defining the ROI (2° in the present case) were extracted. The patterns were fitted with pseudo-Voigt peak functions and third order polynomials accounting for the background. The latter was subtracted from the measured intensity. Furthermore, the intensities were corrected for polarization, which for the almost horizontally polarized high-energy synchrotron beam depends only slightly on 2θ and η. Using the present notations the polarization factor given by Heidelbach *et al.* (1999) reads as

$$P = 1 - \frac{\sin^2 2\theta}{2}(1 - P^* \cos 2\eta), \tag{4}$$

where P^* is the degree of polarization of the primary beam (usually taken as 0.99). At high energies the 2θ diffraction angles are small and polarization correction is generally neglected. Indeed, at $2\theta = 5^\circ$ the difference in P at $\eta = 0$ and 90° is less than 1%, but at $2\theta = 10$ and 15° the difference increases to about 3 and 7%, respectively.

A further correction involves the Lorentz factor, which is generally corrected in 3DXRD (Poulsen, 2004; Offerman & Sharma, 2010):

$$L = \frac{1}{\sin 2\theta |\sin \eta|}. \tag{5}$$

L describes the 2θ and η dependence of the angular velocity of the diffraction vector through the Ewald sphere when the crystal is rotated around the Oz axis. Since L diverges at $\eta = 0$ and 180°, small intervals around these points have been discarded ($\pm 10^\circ$ in η). Owing to the mosaic spread present in deformed crystals, these areas have contributions from sample regions with diffraction vectors close to the inaccessible directions near the rotation axis, representing therefore incomplete information (Poulsen, 2004).

At a photon energy of 63 keV, the absorption of a 1 mm thickness of Al is about 7%. Considering that the diffracting grains are randomly distributed in the illuminated volume of $0.7 \times 0.7 \times 0.6$ mm and that this volume is always in the beam during the 180° rotation, one expects that all texture components are similarly affected by absorption. Therefore, absorption correction was not performed. Pole figures were extracted by dividing the Debye rings into small ROIs corresponding to $\Delta\eta = 2^\circ$ ($= \Delta\omega$) and $2\theta = 0.6^\circ$. The average intensity for each ROI was calculated and was associated with a diffraction vector corresponding to the centre of the $[\Delta\eta, \Delta\omega, \Delta(2\theta)]$ sub-volume. Finally, the integrated intensity was transformed to the pole figure and used as input into the *MTEX* software (Hielscher & Schaeben, 2008) for ODF calculation. The software uses a pole figure inversion method that approximates the unknown ODF by a linear combination of unimodal bell-shaped standard ODFs (Helming *et al.*, 1994). Therefore, the PF points do not have to lie at the nodes of a regular grid and the method is well suited for high-resolution texture evaluation based on area detectors.

2.3. Extraction and analysis of high-resolution radial peaks

2.3.1. Identifying the diffraction peaks of texture components. Extraction of diffraction peaks corresponding to an ideal texture component (*i.e.* for a given orientation matrix $\mathbf{U}$) requires knowledge of the detector angles 2θ and η as well as the rotation ω. The latter can be determined from the Bragg condition. According to equation (2) the first component of $\mathbf{G}_\omega$ can be written as

$$\frac{G_{\omega 1}}{|\mathbf{G}_\omega|} = -\sin\theta. \tag{6}$$

Writing $G_{\omega 1}/|\mathbf{G}_\omega|$ in terms of $\mathbf{G}_\mathrm{S}$ and $\mathbf{\Omega}_z$ we obtain

$$\frac{G_{\omega 1}}{|\mathbf{G}_\omega|} = \cos\omega\gamma_{\mathrm{S}1} - \sin\omega\gamma_{\mathrm{S}2}, \tag{7}$$

where $\gamma_{\mathrm{S}1}$ and $\gamma_{\mathrm{S}2}$ are the direction cosines of $\mathbf{G}_\mathrm{S}$ and can be calculated from equation (1). Equations (6) and (7) transform into a single trigonometric equation

$$a\sin\omega + b\cos\omega + c = 0, \tag{8}$$

where $a = -\gamma_{\mathrm{S}2}$, $b = \gamma_{\mathrm{S}1}$ and $c = \sin\theta$. This equation has no solutions for ω if the angle $\alpha = \measuredangle(\mathbf{G}_\omega, O\mathbf{z})$ (see Fig. 1) is smaller than the Bragg angle θ, one single solution if $\alpha = \theta$ and two solutions {in the $[0, 2\pi)$ interval} if $\alpha > \theta$. The two solutions can be written in closed form:

$$\omega_{1,2} = \arctan\left\{ -\frac{ca^2 \pm b\left[a^2\left(a^2+b^2-c^2\right)\right]^{1/2}}{a\left(a^2+b^2\right)}, \right.$$
$$\left. -\frac{cb \mp \left[a^2(a^2+b^2-c^2)\right]^{1/2}}{(a^2+b^2)} \right\}. \tag{9}$$

It is important to mention that crystallographically equivalent grain orientations $\mathbf{U}' = \mathbf{\Omega}_\mathrm{S}\mathbf{U}$ (where $\mathbf{\Omega}_\mathrm{S}$ is a rotation matrix that preserves the symmetry of the lattice) lead to the same set of ω angles for plane families of the same $\{hkl\}$ type [see equation (1)]. Therefore this set does not depend on the particular choice of the orientation matrix, *e.g.* $(h'k'l')[uvw]$ {where $(h'k'l')$ denotes the Miller indices of the crystallographic plane parallel to ND of the sample frame and $[uvw]$ the crystallographic direction parallel to RD}. This statement is exemplified in Table S2 of the supporting material for two variants {$(123)[63\bar{4}]$ and $(1\bar{3}2)[643]$} of the S3 component.

2.3.2. Evaluation of dislocation density and coherent domain size. In texture measurements, usually no distinction is made between diffraction vectors $\mathbf{H}$, of the same *hkl* type. This is, however, not true in LPA, where owing to the anisotropic strain field of dislocations (causing different broadening of different *hkl*s) a distinction should be made (see *e.g.* Borbély *et al.*, 2000). The analysis should therefore consider a particular $(h'k'l')[uvw]$ orientation to describe the texture component. An indexing example and the interpretation of the broadening of 200-type diffraction spots for the above-

Table 1
Texture components and their 311-type diffraction peaks used for LPA analysis.

The corresponding rotation angle of the turntable ω, the azimuthal angle η, the average dislocation contrast factors $\bar{C}_{hkl}$ and the average geometrical factor $\bar{\Lambda}$ are also indicated.

Texture component	$(h'k'l')[uvw]$	hkl	ω (°)	η (°)	$\bar{C}_{hkl}$	$\bar{\Lambda}$
Cube	(001)[100]	131	22.8	287.6	0.1276	1.10
Goss	(011)[100]	$3\bar{1}1$	119.4	270.0	0.1577	1.36
Copper	(112)[11$\bar{1}$]	$13\bar{1}$	68.2	284.3	0.1421	1.23
Brass	(110)[$\bar{1}$12]	$\bar{1}13$	84.1	270.0	0.1648	1.42
S1	(12$\bar{4}$)[211]	113	103.5	273.8	0.1451	1.25
S2	(123)[41$\bar{2}$]	$\bar{1}\bar{1}3$	8.3	279.1	0.1293	1.12
S3	(123)[63$\bar{4}$]	$11\bar{3}$	52.5	279.1	0.1307	1.13
Dillamore	(4 4 11)[11 11 $\bar{8}$]	$31\bar{1}$	119.6	277.0	0.1364	1.18

mentioned S3 variants (see Table 1 for their definition) is presented in Table S3 of the supporting material.

Peak broadening was analysed in terms of dislocation density and coherent domain size according to Borbély & Groma (2001). This analysis was based on the asymptotic behaviour of the second,

$$M_2(q) = \frac{1}{\pi^2 \varepsilon_F} q - \frac{T}{4\pi^2 K^2 \varepsilon_F^2} + \frac{\Lambda \langle \rho \rangle \ln(q/q_0)}{2\pi^2}, \qquad (10)$$

and fourth,

$$\frac{M_4(q)}{q^2} = \frac{1}{3\pi^2 \varepsilon_F} q + \frac{\Lambda \langle \rho \rangle}{4\pi^2} + \frac{3\Lambda^2 \langle \rho^{(2)} \rangle \ln^2(q/q_1)}{4\pi^2 q^2}, \qquad (11)$$

order restricted moments of the intensity distribution. In these equations $q = 2(\sin\theta - \sin\theta_0)/\lambda$ and represents the distance from the peak centre (in reciprocal space) along the diffraction vector **G**. ε_F is the apparent crystallite size, $\langle \rho \rangle$ is the average dislocation density, and $\Lambda = (\pi/2)G^2 b^2 C_{hkl}$ is a geometrical factor related to the contrast factor of the dislocations C_{hkl} and to the magnitude of the Burgers vector **b**. $\langle \rho^{(2)} \rangle = \frac{1}{2}[\langle \rho^2 \rangle - \langle \rho \rangle^2]$ is the fluctuation of the dislocation density (Groma, 1998). K is the Scherrer constant and T is the taper parameter (Wilson, 1962). The dislocation density was obtained by simultaneously fitting M_2 and $M_4(q)/q^2$. In the latter case, the third term with $\langle \rho^{(2)} \rangle$ in equation (11) was neglected in the regression. The approximation is viable when no maximum in $M_4(q)/q^2$ at low q values is observed (Groma, 1998; Borbély & Groma, 2001; Borbély & Ungár, 2012). q_0 and q_1 in equations (10) and (11) are constants with no physical significance (Groma, 1998). Furthermore, at large q values the logarithmic term in M_2 [equation (10)] is much larger than the middle term containing the taper parameter T, impeding an accurate evaluation of the latter. Therefore, no values of q_0, q_1 and T are presented.

Equations (10) and (11) describe the behaviour of the two moments at large q values. However, the Al–Sc–Zr matrix of the composite contains $Al_3(Sc,Zr)$ precipitates with radii in the 2–24 nm range (Fuller *et al.*, 2003), which because of their coherency with the matrix could perturb the tails of the diffraction peaks (Iida *et al.*, 1988). Indeed, the $Al_3(Sc,Zr)$ precipitates found in Al–Sc–Zr alloys are coherent with the matrix (Marquis & Seidman, 2001), for which reason it is very probable that the observed shoulders on the 311 peaks at relative intensities below 2–3 $\times$ 10^{-2} [marked by arrows in Fig. 3(*a*)] are related to coherency strains. One may attribute the shoulders to the direct scattering from precipitates, which

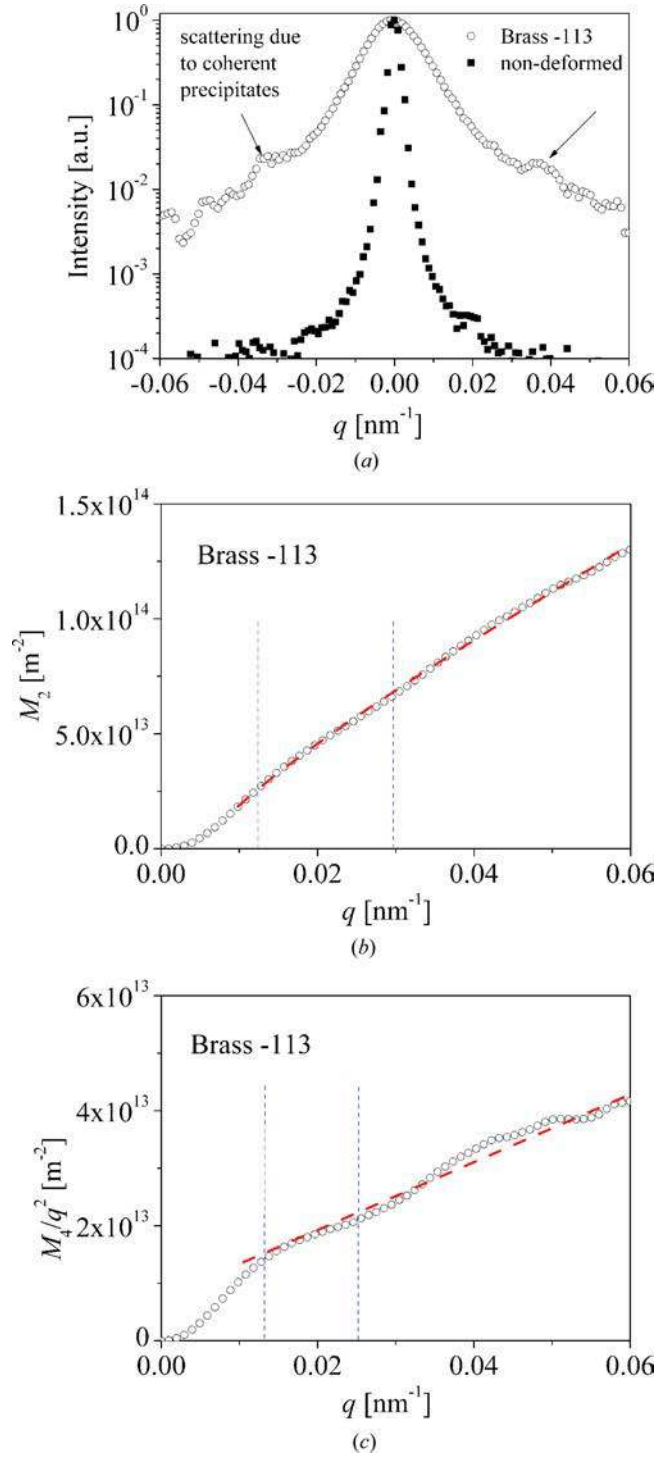

Figure 3
311 peak profiles (*a*) corresponding to the brass texture component of the cold-rolled composite and to the non-deformed Al–0.2Sc–0.1Zr alloy, which characterizes instrumental broadening. The arrows mark the scattering due to coherent precipitates. The second (*b*) and fourth (*c*) order restricted moments of the profile shown in (*a*), which were used for the evaluation of the dislocation density and coherent domain size.

is proportional to the precipitate volume of and the relative difference in the scattering factors of the precipitate and matrix atoms. The direct scattering has a maximum at $q_d = \varepsilon G$, where ε is the internal strain in the precipitate relative to the matrix (Iida *et al.*, 1988) and decays in both directions from q_d. For this reason the evaluation of the moments was limited to $q < q_d$, where scattering from dislocations is more significant. The fit interval is indicated by the vertical dashed lines in Figs. 3(*b*) and 3(*c*). Because the density of precipitates is low (Marquis & Seidman, 2001) compared to that of dislocations, Huang scattering and higher-order contributions (Iida *et al.*, 1988) from the precipitates can be neglected.

In all cases the number of data points considered in the fits was larger than 15. The evaluation was performed by continuously varying the background in steps of 0.1 counts and selecting the value giving the smallest difference between the results of the second and fourth order moments. Instrumental broadening was neglected during the evaluation. As shown in Fig. 3(*a*) the 311 peak corresponding to the non-deformed Al–0.2Sc–0.1Zr alloy is much narrower than the peak of the deformed composite.

3. Results

3.1. Material and experimental conditions

The texture and dislocation density evolution of the major components developed in a cold-rolled Al–0.2Sc–0.1Zr–5 wt%TiB_2 composite (with 72% reduction) was studied during *in situ* annealing. The grain size of the material before rolling was about 25 µm. Elongated brick-shaped specimens having a length of about 20–30 mm along RD and a square cross section of 0.7 × 0.7 mm along TD and ND, respectively, were cut using a low-speed saw from the rolled material. The specimens were mounted with RD along the rotation axis (Oz), while ND was parallel to the incident beam (Ox axis in Fig. 1). This sample positioning on the turntable corresponds to a transformation matrix **S** in equation (1) equal to

$$\mathbf{S} = \begin{pmatrix} 0 & 0 & 1 \\ 0 & 1 & 0 \\ 1 & 0 & 0 \end{pmatrix}. \qquad (12)$$

Before measurements, the samples were electro-polished (to remove the layer influenced by the saw) using the Struers A2 electrolyte at a voltage of 30 V for 20 s. XRD tests were done using a synchrotron beam with a cross section of 1.1 × 0.6 mm in the horizontal and vertical directions, respectively. The specimen was continuously rotated 180° around the Oz axis at an angular speed of 2° s^{-1} and diffraction images were taken every second, which corresponds to integrating the scattered intensity over intervals of $\Delta\omega = 2°$.

The *in situ* annealing experiment consisted of a continuous heating from room temperature (RT) to 823 K at a rate of 5 K min^{-1}. Texture and high-resolution scans were done as follows:

(i) First the texture of the initial cold-rolled state was measured. Positioning the detector at a distance of 734.5 mm from the sample allowed recording of the first five complete diffraction rings (111, 200, 220, 311 and 222) of the Al alloy. A typical diffraction image is presented in Fig. 2(*a*), where in addition to the Debye rings of the Al matrix, the rings of the TiB_2 particles are also visible (indicated by yellow arrows). All five rings of the matrix were used for ODF calculation.

(ii) In the second step the detector was moved to 6 m away from the sample, where it covered only a small region of the 220, 311 and 222 rings (Fig. 2*b*). After the first scan carried out at RT, the sample was heated using an inductive coil. The target temperature was monitored with a thermocouple in contact with the bottom of the sample. Since a temperature gradient may exist in the sample (due to the high heat conductivity of the Al and convection in the open space around the specimen), the real temperature was evaluated

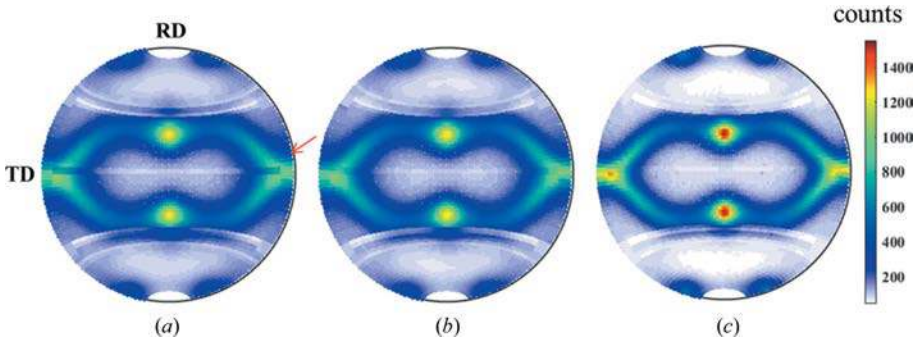

Figure 4
Experimental 111 PFs corresponding to (*a*) the cold-rolled state and the annealed states at (*b*) 573 K and (*c*) 823 K.

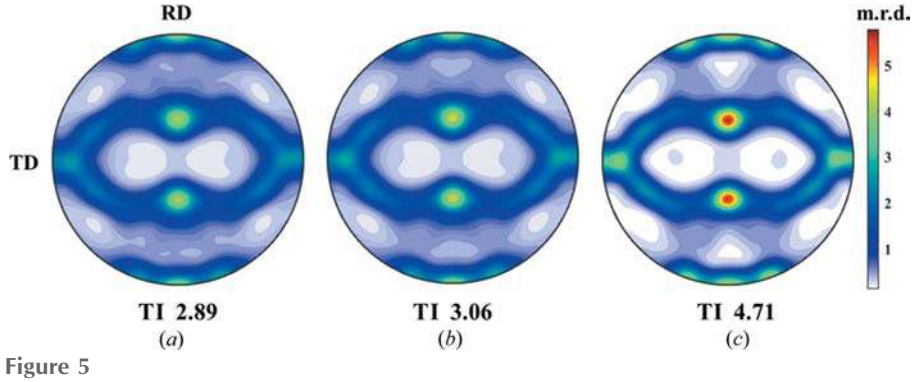

Figure 5
Recalculated 111 PFs corresponding to (*a*) the cold-rolled state and the annealed states at (*b*) 573 K and (*c*) 823 K, with imposed orthorhombic sample symmetry.

from the position of the *hkl* peaks (cell parameter) and the thermal expansion coefficient of the matrix alloy. The latter was determined with an MPD-PRO PANalytical diffractometer equipped with an HTK-1200 Anton Paar furnace in the XRD laboratory of MINES Saint-Etienne. This calibration measurement also showed that the $Al_3(Sc,Zr)$ precipitates are stable to temperatures as high as 873 K (Yuan, 2018). High-resolution patterns were measured every 7 min up to a temperature of 573 K.

(iii) After the scan taken at 573 K the detector was moved to the near field and annealing was further followed by texture scans until 823 K. Scans were taken at 7–8 min intervals.

3.2. Texture evolution

Experimental 111 PFs corresponding to the initial state and the two annealed states at 583 and 823 K are shown in Figs. 4(*a*)–4(*c*), respectively. The white regions around the poles and the great circle on the right-hand side (marked by a red arrow) correspond to the blind regions near the rotation axis [zero solutions of equation (8)]. The white stripes are related to the passive regions between detector modules. The experimental PFs were usually calculated without imposing any sample symmetry. Figs. 5(*a*)–5(*c*) show the PFs recalculated from the ODF with imposed orthorhombic sample symmetry. The intensity distribution in the experimental PFs is not very different from the corresponding recalculated PFs, suggesting that the illuminated volume (of 0.7 × 0.7 × 0.6 mm) captures a statistically significant number of grain orientations. A noteworthy difference exists between the texture indices (TIs) of the initial and the recovered states. The TI, calculated as the integral of the square of the ODF (Bunge, 1982), increases slightly from 3.2 to 3.37 during heating up to 853 K and more significantly to 5.03 at 823 K. Note that the TI increases with ODF resolution, as exemplified in Fig. 6 for ODF steps of 5, 3 and 2°.

3.2.1. Volume fraction evolution of selected texture components. To quantitatively characterize the orientation-dependent recovery of the composite, the volume fractions of typical texture components found in cold-rolled aluminium alloys (Zhou *et al.*, 1991; Kocks *et al.*, 2000; Kühbach *et al.*, 2015) were evaluated. These were determined by integrating the ODF over a 6° disorientation interval around the ideal orientations. The results presented in Fig. 7 indicate that in the deformed state the components with the highest volume fraction are the S1 and Dillamore ($f_V \simeq 3.5\%$). The S3, copper, brass and S2 components can be considered as intermediate ($f_V \simeq 2\%$), while the proportions of cube and Goss are the smallest ($f_V < 0.5\%$). Comparing these values with their corresponding fractions in a random sample (last column of Table 2), it becomes evident that all chosen components (except cube) have higher proportions. The sum of analysed components makes up about 15% of the illuminated sample volume. Usually, ODF integration is performed over 10° disorientation, when the corresponding components have larger proportions. In this case their sum would be 53%. Choosing 6° disorientation (in agreement with the angular intervals chosen for the extraction of high-resolution peaks) requires selecting all components with fractions higher than their threshold value in the random sample, which would lead,

Table 2
The influence of intensity corrections on the volume fraction f_V of different texture components in the initial deformed state.

NC = no correction, LF = Lorentz factor correction and LF + P = Lorentz factor plus polarization correction. All data are in percent. The numbers in parentheses represent the estimated errors of the volume fractions calculated from the difference ODF. $|\Delta f_V|/f_V$ is the relative volume fraction change for the LF + P correction compared to the non-corrected case (NC). The last column gives the volume fractions of a sample with random orientation of grains.

Texture component	$(f_V)_{NC}$	$(f_V)_{LF}$	$(f)_{LF+P}$	$\lvert\Delta f_V\rvert/f_V$	$(f_V)_{Rand}$
Cube	0.09 (20)	0.14 (0.5)	0.14 (0.5)	0.31	0.29
Goss	0.21 (90)	0.35 (1)	0.35 (1)	0.42	0.29
Copper	1.17 (48)	1.66 (1)	1.66 (1)	0.30	0.29
Brass	1.74 (47)	1.68 (38)	1.68 (38)	0.03	0.29
S1	2.95 (143)	3.51 (78)	3.51 (78)	0.16	0.58
S2	1.00 (67)	1.20 (58)	1.20 (58)	0.16	0.58
S3	2.92 (137)	2.46 (92)	2.46 (92)	0.19	0.58
Dillamore	3.11 (111)	3.70 (46)	3.70 (46)	0.16	0.58

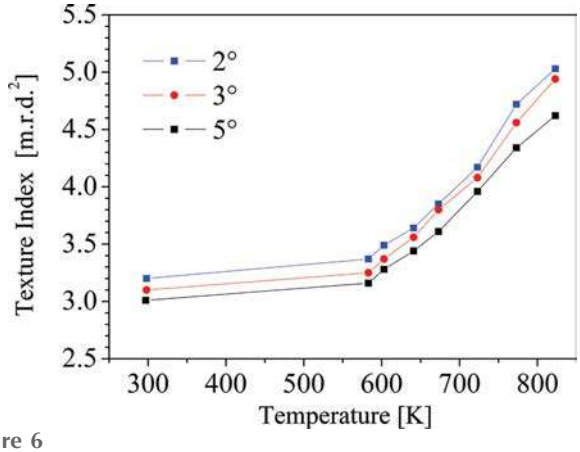

Figure 6
Evolution of the texture index as a function of annealing temperature for different ODF resolutions.

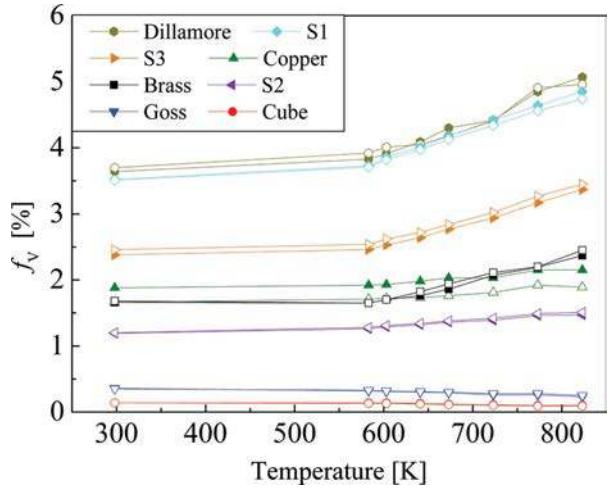

Figure 7
Evolution of the volume fraction of different texture components as a function of time and temperature. The open and filled symbols correspond to ODF resolutions of 2 and 3°, respectively.

Table 3
The influence of ODF resolution on the volume fraction f_V of different texture components.

Texture component	$(f_V)_{5^\circ}$	$(f_V)_{3^\circ}$	$(f_V)_{2^\circ}$	$[(f_V)_{2^\circ} - (f_V)_{5^\circ}]/(f_V)_{2^\circ}$	$[(f_V)_{2^\circ} - (f_V)_{3^\circ}]/(f_V)_{2^\circ}$
Cube	0.18 (1)	0.14 (1)	0.14 (0.5)	−0.31	−0.05
Goss	0.40 (1)	0.36 (2)	0.35 (1)	−0.13	−0.01
Copper	2.12 (1)	1.88 (1)	1.66 (1)	−0.27	−0.12
Brass	1.65 (35)	1.66 (41)	1.68 (38)	0.02	0.01
S1	3.56 (69)	3.52 (73)	3.51 (78)	−0.01	0.00
S2	1.29 (58)	1.19 (51)	1.20 (58)	−0.07	0.01
S3	2.33 (100)	2.38 (94)	2.46 (92)	0.05	0.03
Dillamore	3.47 (34)	3.64 (42)	3.70 (46)	0.06	0.02

however, to a long list in the present case. Therefore, we restrict our analysis only to the main components mentioned in the literature (Kocks *et al.*, 2000).

The evolution of the volume fractions during annealing (Fig. 7) is worthy of note. No substantial changes took place during heating up to 583 K, indicating that dislocation reorganization and subgrain coarsening have relatively small effects on texture. Further heating to 823 K induces, however, significant changes in several components. The fraction of all major components (with $f_V > 1\%$) grew, while that of the minor components slightly decreased (cube and Goss). ODF calculation steps of 2 and 3° (open and filled symbols, respectively) lead to very close results, with the exception of the copper component. To detect significant volume fraction changes their error should be quantified. In texture analysis the ODF error is usually quantified in terms of reliability factors representing a normalized average difference between experimental and recalculated pole figures (Chateigner, 2005). Since texture components can be extracted only from the ODF, determining their error requires an ODF-type error estimator. Therefore, we have calculated a 'difference ODF' from the absolute value of the difference between the recalculated PFs and normalized experimental PFs. Because of error accumulation in the difference ODF, the error measure introduced on this basis will be much larger than the true error of the volume fractions, but it can be useful as a rough estimate. Their values for the different components characterizing the initial state are shown in parentheses in Table 2. In most cases, the error is proportional to the volume fraction and does not depend much on the ODF resolution. The calculations have shown that the uncertainty obtained from the difference ODF (Table 2) is usually larger than volume fraction differences corresponding to ODF resolutions of 5 and 2° (Table 3). The latter table also indicates that an ODF resolution of 3° leads to very good agreement with results obtained from the highest available resolution of 2°. An exception is the copper component, which has a relative decrease of 12%, indicating that it has more spread than the other components. As a result of this property, the usual 5° resolution leads to about 30% relative error for its volume fraction.

3.3. Dislocation density evolution of different texture components

The selection of diffraction vectors of different texture components for LPA analysis should avoid their overlap. The PFs with superposed poles corresponding to the chosen texture components can be very helpful for this purpose. An example is shown in Fig. S1 in the supporting material, which indicates in addition the expected relative intensity of high-resolution peaks, an important criterion in the selection process. Since texture extraction is quite fast (∼1 min), peak selection can be done during the available synchrotron beam time. In the present case (see the positions of the small circles in Fig. S1) most of the poles (except for the cube and Goss) are located in regions of relatively high density, which guarantee a fast measurement.

The evolution of 311-type peak profiles of the S1 and Goss components as a function of temperature is shown in Figs. 8(*a*) and 8(*b*), respectively. A narrowing of the peaks with annealing time is visible. The variation of the FWHM of the 311 peaks of all texture components is shown in Fig. 9(*a*) as a function of temperature and annealing time. The peak widths remain constant until about 408 K (indicated by a vertical

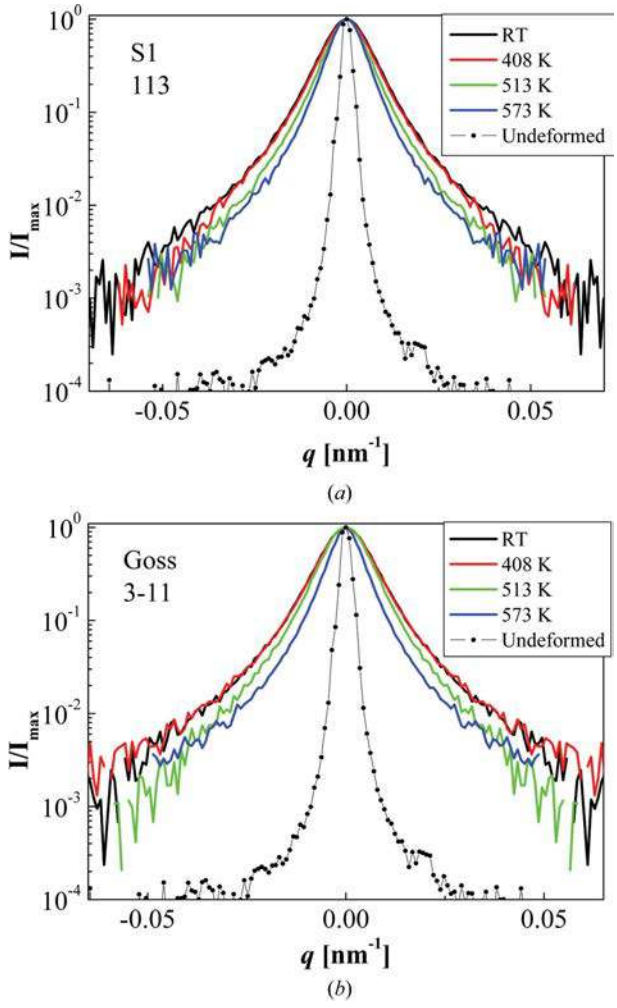

Figure 8
Evolution of 311-type peak profiles of (*a*) the S1 and (*b*) the Goss texture component at different temperatures. The narrowing of the peaks during annealing is visible.

dashed line), when recovery begins. After this point the peak widths decrease linearly and homogeneously for all components. In general, texture components with initially higher/lower widths at RT show the same relationships at 573 K, too.

Recovery of the microstructure was analysed according to LPA in terms of dislocation density and coherent domain size. The evaluation of these parameters was performed as described in §2.3.2, by fitting a line to the intermediate-q region of the fourth order moment (M_4/q^2), and the nonlinear equation (10) to the second order moment. The slope and the intercept of the line fitted to M_4/q^2 are inversely and linearly proportional to ε_F and $\langle\rho\rangle$, respectively. Fig. 9(b) shows a significant decrease of the intercept and slope of the fitted lines with heating. ε_F and $\Lambda\langle\rho\rangle$ were calculated as the average of the fit values obtained from the second and fourth order moments. The average dislocation contrast factor $\bar{C}_{hkl}$ (and $\bar{\Lambda}$) was estimated (Table 1) from the results of crystal plasticity calculations using a Taylor model with relaxed strain rate components (Fortunier & Driver, 1987). The relative dislocation population of the slip systems was considered proportional to the amount of the slip on the corresponding system, which was obtained from the crystal plasticity simulation (Borbély *et al.*, 2000; Guiglionda *et al.*, 2004). We mention, however, that a more realistic estimation of dislocation populations and consequently a more accurate average contrast factor $\bar{C}_{hkl}$ can be obtained from models explicitly incorporating the dislocation density into the constitutive equations of crystal plasticity (Beyerlein & Tomé, 2008). Furthermore, it was assumed that half of the dislocations are screw and half are of edge type. The contrast factor of single dislocations was calculated with the *ANIZ-C* program (Borbély *et al.*, 2003). The evolution of $\langle\rho\rangle$ and ε_F for the analysed texture components is shown in Figs. 10(a) and 10(b), respectively, as a function of temperature and time. Both the dislocation density and coherent domain size remain constant (within the evaluation error) up to a temperature of about 408 K, after which they decrease and increase, respectively. Interestingly, $\langle\rho\rangle$ for all components varies at similar rates. A similar uniform variation was also found for ε_F at the

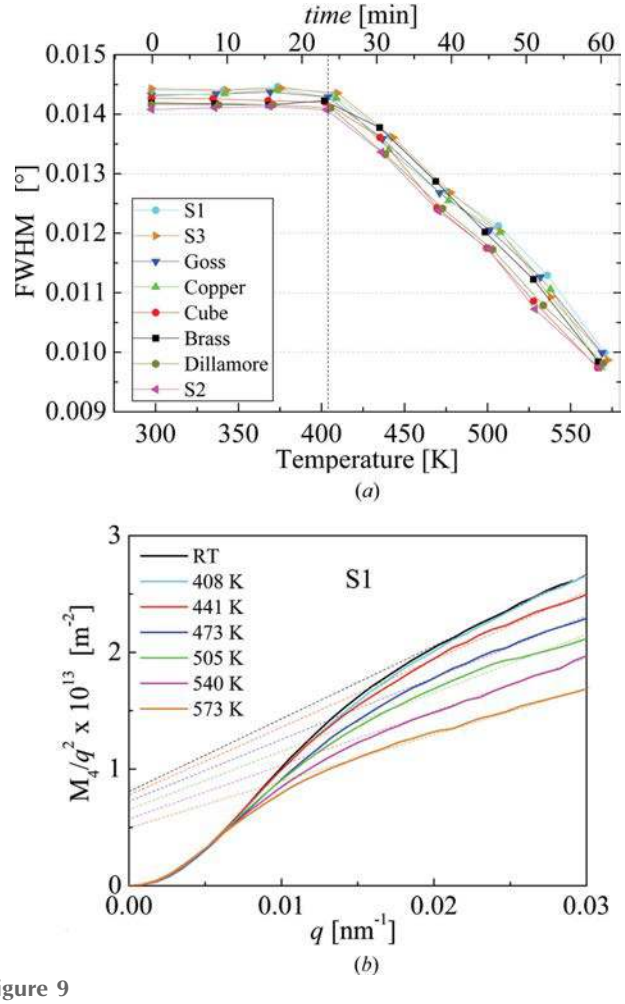

Figure 9
(a) Variation with time and temperature of the FWHM of the 311-type peaks corresponding to the selected eight texture components. (b) Fourth order restricted moments of the 113 peaks of the S1 component (Fig. 8a) at different temperatures. The intercept of the fitted lines is proportional to $\Lambda\langle\rho\rangle$ and the slope to ε_F [equation (11)].

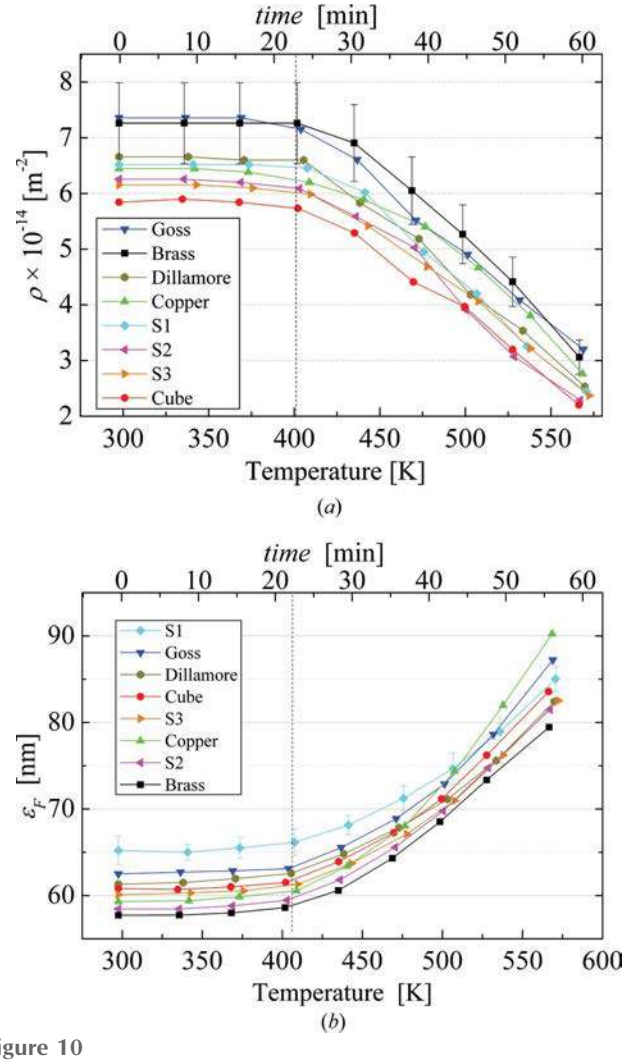

Figure 10
Variation of dislocation density $\langle\rho\rangle$ (a) and apparent crystallite size ε_F (b) of the analysed texture components as a function of time and temperature. The analysed profiles correspond to the peaks given in Table 1.

beginning of recovery. However, at later stages the growth rate of the Goss and copper components was significantly larger.

4. Discussion

4.1. Influence of intensity corrections on the volume fraction of the texture components

Recovery of plastically deformed crystals takes place by the annihilation and rearrangement of dislocations into low-energy structures (Humphreys & Hatherly, 2004). It is an intriguing question if these mechanisms lead to noticeable texture changes or not. Their detection requires, therefore, a very accurate ODF, for which reason all complete Debye rings (111, 200, 220, 311 and 222) were used for ODF determination. Furthermore, the correct intensities are needed, which involves correcting for the parameters affecting the measurement. From this point of view the advantage of high-energy X-rays becomes obvious, since intensity corrections are minimal. The most noticeable defocussing correction applicable to laboratory data disappears because the irradiated volume is constant. As the energy of the X-rays is increased, the absorption correction becomes less and less significant. The results of the present data set (for the utilized material and diffraction conditions) shown in Table 2 evidence that the most important correction concerns the Lorentz factor, which affects the scattered intensity through the angular speed at which a given reciprocal lattice point traverses the Ewald sphere. The integrated intensity for the case of a rotation axis perpendicular to the diffraction vector was treated by Warren (1990). However, the general case for an oblique rotation axis contains an additional $1/|\sin\eta|$ factor (Poulsen, 2004), which according to the present results significantly changes the volume fraction of most components. As expected, the effect of polarization at this high photon energy is negligible. According to Table 2 the error of the volume fractions as obtained from the difference ODF decreases after Lorentz correction, indicating a more coherent data set.

The absorption of Al at 63 keV is not completely negligible (about 7% for a thickness of 1 mm) and can influence the final result. Accurate correction requires knowledge of the position of the grains in the sample, which is only available in 3DXRD. To obtain a more accurate intensity for the texture components we have used a large rotation interval of $\omega = 180^\circ$, during which all *hkl* planes will diffract once. Therefore, using *hkl* poles of higher multiplicity can lead to a better absorption correction.

4.2. Recovery behaviour of different texture components

A first qualitative description of the microstructure of different texture components is obtained from the variation of the FWHM as a function of temperature (Fig. 9*a*). On the basis of computer simulations, Kalácska *et al.* (2017) have shown recently that the FWHM depends not only on dislocation density (and the coherent domain size) but also on the dislocation arrangement, making impossible an accurate evaluation of the dislocation density from the FWHM alone. However, its behaviour as a function of temperature reflects qualitatively the changes taking place in the microstructure. It is evident that recovery in each texture component starts around 408 K and has the same rate for all. Texture components having a higher width in the initial deformed state usually have larger widths at 573 K, too.

Deeper insight into microstructural changes taking place during recovery is given by Figs. 10(*a*) and 10(*b*), showing the variation of the dislocation density and coherent domain size, respectively. The difference in dislocation density among the studied components is relatively small. The maximum and minimum values are within 12% from the average, which is equal to their error (10–15%). Therefore, we conclude that recovery induces uniform dislocation annihilation independent of the crystallographic orientation of the grains in the composite and their specific dislocation structures.

The highest dislocation density was found in the Goss and brass components, a result which is different from previous literature data obtained by Guiglionda *et al.* (2004) for hot-plane-strain-deformed Al–2.5Mg alloy, where the S1 and copper components had the highest value, while the cube component had the lowest. For the composite studied here the cube component also had the lowest density, indicating its sensitivity to recovery and dynamic recrystallization. The dynamic recrystallization hypothesis of the composite is strengthened by results obtained on the Al–0.2Sc–0.1Zr base alloy, cold rolled to similar reduction, which had a higher dislocation density than the composite (Yuan, 2018). Because of the presence of TiB_2 particles in the composite, one may expect that the composite recrystallizes at smaller rolling strains than the unreinforced alloy. Both materials, however, develop a similar texture, indicating that major slip activity takes place on the same systems. Another difference, besides the higher dislocation content of the alloy, is related to a higher heterogeneity of the dislocation density among the different components (Yuan, 2018). Heterogeneity has also been observed among the texture components of the hot-deformed Al–2.4Mg alloy (Guiglionda *et al.*, 2004), where the relative difference between the maximum and minimum values was about 50% compared to only 25% for the Al–0.2Sc–0.1Zr–TiB_2 nanocomposite.

The coherent domain sizes shown in Fig. 10(*b*) also present similar tendencies for all texture components. Like the variation of the FWHM and dislocation density, the beginning of recovery affects the coherent domain sizes too, which start to increase from temperatures of about 408 K (indicated by the vertical dashed line). Their growth rate is similar at low temperatures, but it becomes more heterogeneous at higher temperatures.

Interestingly, the Goss component has a high dislocation density and domain size. Conversely, the brass component has high dislocation density and the lowest coherent size. These differences are similar to the results of Albou *et al.* (2011) for plane-strain-compressed Al–0.1Mn single crystals of Goss and brass orientation. The electron backscatter diffraction (EBSD) results of Albou *et al.* (2011) indicate that the spread of local disorientations in the Goss component is larger than in

the brass, which according to the Humphreys (1997) model, stating that subgrains with higher disorientations grow faster, could explain the larger domains found in the Goss component at the initial state (after dynamic recovery) and also the higher growth rates during heating to 573 K.

4.3. Influence of subgrain/grain coarsening on texture

As discussed in §4.1, dislocation annihilation and rearrangement into low-energy structures during recovery led only to minimal changes in the volume fraction of the different texture components. Heating above 573 K, however, induced a significant increase in almost all components, excepting the cube and Goss, which experienced a slight decrease. The underlying mechanism for these changes should include, besides dislocation rearrangement, subgrain and grain coarsening. It is known that the presence of second phase particles increases the fraction of high-angle boundaries during deformation, which can lead to the continuous recrystallization of the composite as demonstrated by the same rolling-type texture being preserved at 823 K. Furthermore, EBSD analysis of a sample heated to 823 K (Yuan, 2018) shows that 85% of the composite grains have no internal structure (no subgrains with disorientations larger than 0.3°), which confirms that continuous recrystallization occurred. Therefore, grain coarsening should be considered in the interpretation of texture results. According to Fig. 7, texture components with higher fraction seem to grow at a higher rate. However, the relative changes from RT to 823 K (the f_V change normalized by the volume fraction at RT) are about 0.4 for most of the growing components, excepting copper and S2, which have lower values of about 0.2.

5. Conclusions

A method for combined measurement of crystallographic texture and high-resolution diffraction peaks corresponding to different texture components has been presented. The technique exploits the high penetration power of the hard X-ray radiation and the versatile setup available at ID31 of the ESRF. Rapid movement of the detector from close to far distances from the specimen enables a simple and fast change between the low- and high-resolution modes.

Texture measurement in low-resolution mode was described and the main corrections affecting the ODF were discussed. For the conditions used in the present experiment the most significant correction was introduced by the Lorentz factor, which changed the relative proportion of the Goss and copper components by about 50%. The polarization correction was negligible, while absorption effects were minimized by increasing the rotation interval and measuring the contribution of all diffracting planes. It was emphasized that high-energy X-rays enable fast and accurate high-resolution texture characterization, a technique which can be placed between classical laboratory methods and the general 3DXRD. It allowed us to study the influence of the ODF resolution on the volume fraction of different texture components. The results show the classical 5° resolution and lead to relative differences of up to 30% for components with large spread.

LPA of high-resolution diffraction peaks showed that the heterogeneity of the dislocation structure in the cold-rolled Al–0.2Sc–0.1Zr–5 wt%TiB_2 nanocomposite is lower compared to a hot-deformed Al–2.5Mg alloy (Guiglionda *et al.*, 2004). It was also shown that recovery of the composite from RT to 573 K takes place in a nearly homogeneous way, all texture components recovering at similar rates.

Continuous recrystallization during heating from 408 to 823 K took place. The Dillamore, S1, S3 and brass components showed a higher relative growth (∼0.4), the S2 and copper components had intermediate values (∼0.2), and the Goss and cube components slightly decreased. The statistically relevant results obtained in this work can be used for targeted local EBSD studies for understanding the continuous recrystallization mechanisms and for setting up annealing strategies that meet the requirements of specific industrial applications.

Acknowledgements

HY and AB acknowledge the support of ESRF for beamtime allocation under the proposals MA2920 and MA5139.

Funding information

HY acknowledges the financial support of the China Scholarship Council (scholarship No. 201406230026). AB acknowledges the financial support of the Labex MANUTECH SISE of the University of Lyon.

References

Albou, A., Borbély, A., Maurice, C. & Driver, J. H. (2011). *Philos. Mag.* **91**, 3981–4000.

Beyerlein, I. J. & Tomé, C. N. (2008). *Int. J. Plast.* **24**, 867–895.

Borbély, A., Dragomir-Cernatescu, J., Ribárik, G. & Ungár, T. (2003). *J. Appl. Cryst.* **36**, 160–162.

Borbély, A., Driver, J. H. & Ungár, T. (2000). *Acta Mater.* **48**, 2005–2016.

Borbély, A. & Groma, I. (2001). *Appl. Phys. Lett.* **79**, 1772–1774.

Borbély, A. & Ungár, T. (2012). *C. R. Phys.* **13**, 293–306.

Borbély, A., Renversade, L., Kenesei, P. & Wright, J. (2014). *J. Appl. Cryst.* **47**, 1042–1053.

Brokmeier, H. G. & Yi, S. (2017). *Neutrons and Synchrotron Radiation in Engineering Materials Science: From Fundamentals to Applications*, 2nd ed., edited by P. Staron, A. Schreyer, H. Clemens & S. Mayer, pp. 55–72. Weinheim: Wiley-VCH Verlag.

Bunge, H. J. (1982). *Texture Analysis in Materials Science*. London: Butterworths.

Busing, W. R. & Levy, H. A. (1967). *Acta Cryst.* **22**, 457–464.

Chateigner, D. (2005). *J. Appl. Cryst.* **38**, 603–611.

Csiszár, G., Pantleon, K., Alimadadi, H., Ribárik, G. & Ungár, T. (2012). *J. Appl. Cryst.* **45**, 61–70.

Fortunier, R. & Driver, J. H. (1987). *Acta Metall.* **35**, 1355–1366.

Fuller, C. B., Seidman, D. N. & Dunand, D. C. (2003). *Acta Mater.* **51**, 4803–4814.

Groma, I. (1998). *Phys. Rev. B*, **57**, 7535–7542.

Groma, I., Ungár, T. & Wilkens, M. (1988). *J. Appl. Cryst.* **21**, 47–54.

Guiglionda, G., Borbély, A. & Driver, J. H. (2004). *Acta Mater.* **52**, 3413–3423.

Heidelbach, F., Riekel, C. & Wenk, H.-R. (1999). *J. Appl. Cryst.* **32**, 841–849.
Helming, K., Schwarzer, R. A., Rauschenbach, B., Geier, S., Leiss, B., Wenk, H.-R., Ullemeyer, K. & Heinitz, J. (1994). *Z. Metallkd.* **85**, 545–553.
Hielscher, R. & Schaeben, H. (2008). *J. Appl. Cryst.* **41**, 1024–1037.
Honkimäki, V. (2016). *ID31 – High-Energy Beamline for Buried Interface Structure and Materials Processing*, http://www.esrf.eu/UsersAndScience/Experiments/StructMaterials/ID31.
Humphreys, F. J. (1997). *Acta Mater.* **45**, 4231–4240.
Humphreys, F. J. & Hatherly, M. (2004). *Recrystallization and Related Annealing Phenomena*, 2nd ed. Oxford: Elsevier.
Iida, S., Larson, B. C. & Tischler, J. Z. (1988). *J. Mater. Res.* **3**, 267–273.
Kalácska, Sz., Groma, I., Borbély, A. & Ispánovity, P. D. (2017). *Appl. Phys. Lett.* **110**, 091912.
Kocks, U. F., Tomé, C. N. & Wenk, H.-R. (2000). *Texture and Anisotropy: Preferred Orientations in Polycrystals and Their Effect on Materials Properties*. Cambridge University Press.
Kühbach, M., Brüggemann, T., Molodov, K. D. & Gottstein, G. (2015). *Metall. Mater. Trans. A*, **46**, 1337–1348.
Kužel, R. & Klimanek, P. (1988). *J. Appl. Cryst.* **21**, 363–368.
Marquis, E. A. & Seidman, D. N. (2001). *Acta Mater.* **49**, 1909–1919.
Moscicki, M., Kenesei, P., Wright, J., Pinto, H., Lippmann, T., Borbély, A. & Pyzalla, A. R. (2009). *Mater. Sci. Eng. A*, **524**, 64–68.
Oddershede, J., Schmidt, S., Poulsen, H. F., Sørensen, H. O., Wright, J. & Reimers, W. (2010). *J. Appl. Cryst.* **43**, 539–549.
Offerman, S. E. & Sharma, H. (2010). *In-situ Studies with Photons, Neutrons and Electrons Scattering*, edited by T. Kannengiesser, S. S. Babu, Y. Komizo & A. J. Ramirez, pp. 41–72. Cham: Springer.
Poulsen, H. F. (2004). *Three-Dimensional X-ray Diffraction Microscopy. Mapping Polycrystals and their Dynamics.* Springer Tracts in Modern Physics, Vol. 205. New York: Springer.
Renversade, L. & Borbély, A. (2017). *J. Appl. Cryst.* **50**, 1144–1157.
Tang, Y., Chen, Z., Borbély, A., Ji, G., Zhong, S. Y., Schryvers, D., Ji, V. & Wang, H. W. (2015). *Mater. Charact.* **102**, 131–136.
Warren, B. E. (1990). *X-ray Diffraction*, p. 41. Mineola: Dover Publications.
Wauthier-Monnin, A., Chauveau, T., Castelnau, O., Réglé, H. & Bacroix, B. (2015). *Mater. Charact.* **104**, 31–41.
Wilson, A. J. C. (1962). *Proc. Phys. Soc.* **80**, 286–294.
Yuan, H. (2018). PhD thesis, MINES Saint-Etienne, France.
Zhou, Y., Neale, K. W. & Tóth, L. S. (1991). *Acta Metall. Mater.* **39**, 2921–2930.